How do zeolite-templated carbons grow?

Thibaud Aumond, Isabelle Batonneau-Gener, Yannick Pouilloux, Ludovic Pinard, Dorothea Wisser, Myriam Moreau, Hervé Vezin, Alain Moissette, Alexander Sachse

How do Zeolite-Templated Carbons Grow?

Thibaud Aumond,[a] Isabelle Batonneau-Gener,[a] Yannick Pouilloux,[a] Ludovic Pinard,[a] Dorothea Wisser,[b] Myriam Moreau,[c] Hervé Vezin,[c] Alain Moissette,[c] Alexander Sachse[a]*

[a]Institut de Chimie des Milieux et Matériaux de Poitiers (IC2MP), Université de Poitiers – UMR 7285 CNRS, UFR SFA, Bat. B27, 4 rue Michel Brunet, TSA 51106, 86073 Poitiers, Cedex 9, France.

[b]Erlangen Center for Interface Research and Catalysis, Friedrich-Alexander-Universität Erlangen-Nürnberg, Egerlandstrasse 3, 91058 Erlangen, Germany.

[c]Laboratoire de Spectroscopie pour les Interactions la Réactivité et l'Environnement Université de Lille, UMR CNRS 8516-LASIRE, 59000 Lille, France.

*corresponding author: alexander.sachse@univ-poitiers.fr

Abstract

Major insights into the formation mechanism of zeolite-templated carbons (ZTCs) were achieved via a thorough *ex situ* kinetic study of the hybrid (carbon/zeolite) and carbon materials. In depth characterization of the chemical, electrical, textural and morphological properties of the materials allowed us to draw a precise picture of the key steps of the ZTC formation. An *in situ* time resolved GC study enabled us to achieve complementary insights on the ethylene consumption and hydrogen production during ZTC synthesis. Three stages could be disclosed: nucleation, growth and condensation. During nucleation, individual polyaromatic hydrocarbons (PAHs) develop through the aromatization of ethylene. These PAHs present high spin concentration and react upon zeolite dissolution, leading to unstructured carbon particles of undefined morphology. These carbons feature persistent radicals. During growth the PAHs evolve to form more complex rylene-type molecules. Typical structural, textural and morphological features of ZTCs start to emerge during this second stage. The evolution of electrical conductivity of hybrid materials indicates partial condensation of PAHs throughout the zeolite crystals leading to their connection. The carbon materials achieved during the second stage can be described as composites of ZTCs and randomly reacted PAHs. Condensation, which is importantly induced by heat treatment, triggers full connection of the ZTC network. Textural, morphological, structural, and electrical features develop, which result directly from zeolite templating. Final ZTCs feature carbonyl functionalization, which is inherent to the zeolite dissolution step and probably results from radical quenching with water.

Keywords: zeolite-templated carbon, ZTC, mechanism, kinetic, formation, growth, ***BEA**, radical.

1. Introduction

A resurgence of interest in porous carbon frameworks synthesized within sacrificial zeolite templates, also known as zeolite-templated carbons (ZTCs), has recently occurred. The growing interest in ZTC science is related to their unique properties combining tailored microporosity and electrical conductivity making them promising materials for numerous applications including hydrogen and methane storage, electrochemical capacitors and fuel cells [1]. Their first synthesis was achieved by Kyotani and coworkers in 1997 who attempted to synthesize a new type of regular microporous carbon [2]. The term ZTC was employed for the first time by Su *et al.* seven years later [3], while suggested since the very beginning of the present century [4]. These carbon materials have been described as curved graphene sheets by Kyotani and coworkers [5] and thereafter they were claimed to present Schwarzite structure [6]. This latter assumption has yet strongly been questioned [7].

ZTCs are achieved through the polymerization of carbon precursors within the microporous system of a sacrificial zeolite template. Various zeolite structures have been claimed to allow for the development of ZTCs, including small and medium pore size zeolites, such as those featuring **LTA** or **MFI** structures [8,9]. Large pore zeolites with interconnected 3D micropore systems are the most suited templates for high quality ZTC synthesis [1]. Only three zeolites feature these structural requirements, *i.e.* **FAU**, **EMT** and ***BEA**. In **FAU** and **EMT** the interconnected microporous network results from the connection of cages through 12 membered ring (MR) windows. ***BEA** features a 12-ring pore channel system in *a* and *b* (6.6 × 6.7 Å), which intersections result in a further 12-ring channel in *c* (5.6 × 5.6 Å).

Various atomistic structural models have been proposed for ZTCs resulting from the **FAU** framework, based on computational simulation and classified into two main families: open blades and closed struts [4]. ZTCs resulting from beta zeolite (***BEA**) were simulated as a

structure of connected carbon nanotubes [10] and more recently as a network of partially disconnected carbon nanoribbons [11].

The impact of different textural and chemical properties of the zeolite template have been reported in ZTC synthesis, such as the nature of the counterion [1,12], the crystal size [11,13,14] and the presence of mesopores [15]. Likewise, different carbon sources have been tested in the quest for achieving high quality ZTCs, such as liquid (*e.g.* furfuryl alcohol) or gaseous (*e.g.* ethylene, acetylene) precursors [1]. Ethylene revealed as the carbon precursor of choice due to its lower hazardousness compared to acetylene and reduced diffusional limitations compared to bulkier carbon-based molecules.

Generally, ZTC synthesis is carried out on activated zeolites under diluted carbon gas precursor flow at temperatures between 600 and 800 °C for 2 to 6 h. This first step is frequently described as chemical vapor deposition (CVD). This designation is yet unfortunate as the zeolite importantly impacts the carbon formation process and cannot be regarded as an inert substrate. This first synthesis step is often followed by a second step at higher temperature under inert gas flow, which is known as heat treatment. The final ZTC is then obtained after dissolution of the zeolite from the hybrid material, classically through a hydrofluoric acid treatment.

Despite the growing interest in ZTC science, rather little is known about their formation mechanism and on the key steps that govern their synthesis. Only few reports have been published that attempt at describing in detail the formation mechanism of ZTCs using zeolite X (**FAU** structure) as template [16,17]. Liu *et al.* [16] recently reported an *in situ* mass spectroscopy observation of ethylene decomposition products, mainly H_2, CH_4 and C_6H_6, during the development of ZTCs in zeolite X at 600 °C. Based on *in situ* thermogravimetric analysis (TGA) the authors further claimed to identify three stages of the process: (*i*) an initial fast stage, in which carbon deposition is high, (*ii*) an intermediate stage in which carbon

deposition is slower due to increased mass transfer resistance of ethylene, and (*iii*) a final slow stage in which carbon uptake is very weak. A previous report by Nishihara and co-workers [17] already suggested these stages based on the observation of TGA mass gain. The authors concluded the formation of nano-graphene entities during the ethylene induction period within the zeolite pores, which are connected during the heat treatment step. Yet, major questions prevail related to the evolution of the chemical and structural properties of the developing ZTC in order to completely describe their synthesis mechanism.

The present contribution reports a systematic *ex situ* kinetic study of the evolution of the key properties of the developing ZTC using beta zeolite (***BEA** structure) as template. The sound characterization of chemical, electrical, textural and morphological properties of both the hybrid and resulting carbon materials allowed us to draw a full picture of the ZTC evolution. Three stages were disclosed and identified as nucleation, growth and condensation of polyaromatic hydrocarbons.

2. Experimental section

2.1 Materials

Tetraethylammonium hydroxide (TEAOH, 35% in water, Fisher Scientific), aluminum (99.5%, Alfa Aesar), tetraethylorthosilicate (TEOS, Merck), hydrofluoric acid (49% in water, Fisher Scientific), sodium bicarbonate (Sigma Aldrich, 99%), boric acid (Sigma Aldrich, 99%), ethylene (>99.9% Air Liquide), and nitrogen (99.995%, Air Liquide) were purchased and used as received.

2.2 Synthesis of the zeolite template

The zeolite template was synthesized following an adapted protocol [18]. 0.6 g of aluminum were stirred in 45.92 g of TEAOH at room temperature for 24 hours until total dissolution of the powder. 33.28 g of TEOS were added to the solution under stirring until complete evaporation of the ethanol and yielding of a white and viscous gel. 17.28 g of deionized H_2O were added to the gel followed by the addition of 4 mL of aqueous HF solution. The solution was stirred for 4 hours at room temperature and transferred to a Teflon lined stainless steel autoclave and heated at 170 °C for 14 days under static conditions. A white powder was recovered using centrifugation, which was abundantly washed with deionized water. After a drying step at 80 °C for 16 hours, the powder was calcined at 550 °C for 6 hours.

2.3 Kinetic study on the formation of ZTCs

2.3.1 Hybrid materials

A flow setup as previously described was used for the kinetic study of the formation of ZTCs [15]. For each experiment, 1.5 g of the template beta zeolite was placed in a cylindrical quartz reactor containing a frit and activated in a tubular furnace at 150 °C for 1 hour and 690 °C for an additional hour under a nitrogen flow of 150 mL min^{-1}. The gas was then switched to a mixture of 6.67 vol% C_2H_4 in N_2 for the indicated synthesis time (5, 10, 15, 30, 45, 60, 90, 120, 180 and 240 min) and the reactor was cooled to room temperature (RT) under N_2. For the experiment 240 min+HT the temperature was raised after 240 min to 890 °C and kept at this temperature for 2 hours under N_2 flow before cooling to RT.

2.3.2 Carbon materials

The carbon materials were achieved from each hybrid material after the complete dissolution of the zeolite. 1 g of the hybrid compound was transferred to a Teflon beaker and stirred with 10 mL of aqueous HF solution for 4 hours at room temperature. In order to neutralize the fluoride, 60 mL of a saturated aqueous H_3BO_3 solution was added. The mixture was then neutralized by adding 60 mL of a saturated aqueous $NaHCO_3$ solution. After 1 hour of stirring at RT, the carbon materials were recovered by filtration and abundantly washed with hot deionized water and thereafter dried at 80 °C for 12 h.

2.4 Characterization of hybrid and carbon compounds

The structural packing density (SPD) was determined by thermogravimetric analysis (TGA) using a SDT Q600 Waters device under air with a flow of 100 mL min^{-1}. The sample was heated to 900 °C with a ramp of 10 °C min^{-1}. SPD corresponds to the mass of carbonaceous species per gram of zeolite ($g_C\ g_{Zeo}^{-1}$) and was calculated using equation 1.

$$SPD = \frac{m_c}{m_Z} \qquad (1)$$

Where m_C and m_Z are the mass of carbonaceous species (*i.e.* mass loss in TGA between 500 – 700 °C) and zeolite, respectively (**Figure S1**).

The maximal combustion temperature was calculated from differential temperature analysis (DTA) and corresponds to the value for which the DTA signal reached a maximum.

Nitrogen physisorption was carried out using a Micromeritics 3Flex at 77 K. Approximately 50 mg of sample were outgassed at 300 °C for 12 h before the measurement. Microporous volumes and specific surface areas were calculated through the *t*-plot method. The thickness of the nitrogen layer was calculated using reference isotherms of (*i*) a non-porous silica (used for the *t*-plot of zeolites) and (*ii*) graphene (used for the *t*-plot of carbons) [15]. Pore size

distributions were determined using non-linear density functional theory (NLDFT) models available on SAIEUS software. For the zeolites an NLDFT model developed for zeolitic materials was applied and a 2D-NLDFT model developed for carbon materials with heterogeneous structure was used for the carbon materials. The apparent density of hybrid compounds (ρ_{App}) is a function of the SPD and of the occupied zeolite micropore volume and was calculated using equation 2 and is given as the ratio between the mass of carbonaceous species and its volume in the hybrid material ($g_C\ cm^3$).

$$\rho_{App} = \frac{SPD}{V_{micro_i} - V_{micro_f}} \quad (2)$$

Where $Vmicro_i$ corresponds to the micropore volume of the zeolite template and $Vmicro_f$ to the micropore volume of the hybrid material at a given synthesis time.

X-ray powder diffraction (XRD) patterns were collected using a PANalytical Empyrean X-ray diffractometer using CuKα radiation (1.54059 Å) from 5 to 50 °2θ. Elemental analysis allowed to quantify atomic amounts of carbon, hydrogen and oxygen in both hybrid and carbon materials and was performed using a Flash EA 1112/Flash 2000 Thermo instrument. Zeolite composition was determined using ICP-OES analysis using a Perkin Elmer Optima 2000 DV apparatus. Scanning electron microscopy (SEM) images were obtained using a JEOL JSM-790CF microscope and transmission electron microscopy (TEM) images using a JEOL 2100 instrument (operating at 200 kV with LaB_6 source and equipped with Gatan Ultra scan camera). Raman spectra were obtained using two excitation wavelengths. For the visible 532 nm wavelength, a LabRam HR 800-UV Horiba Jobin Yvon confocal microscope equipped with a Peltier cooled CCD detector was used with the application of a diffraction grating with 600 lines mm^{-1} and a confocal hole of 200 µm. Raman spectra were further recorded at 266 nm on a LabRam HR 800 UV spectrometer (Horiba scientific) equipped with a back-illuminated CCD detector. The 800 mm focal length system was equipped with a 266

nm laser (Coherent) focused with a 80X (NA 0.55) objective on the sample. The measured spatial resolution is 0.5 µm. The use of a 2400 g mm^{-1} grating permits one to reach a 1.7 cm^{-1} per pixel spectral resolution.

Electrical conductivity was measured with a Solartron 12962A sample holder associated with a Solartron SI 1287 electrochemical interface and an SI 1260 impedance/gain-phase analyzer. Powder samples were crushed and introduced between two gold disk electrodes of 10 mm diameter. Distance between electrodes was measured with a micrometer and was typically comprised between 0.2 and 0.6 mm. The ohmic resistance was measured by impedance spectroscopy at 0 V bias with 10 mV amplitude from 100 kHz to 1 Hz. The ohmic resistance value was taken for a 0° phase shift when no imaginary contribution occurred. Each conductivity value resulted from triplicates with a relative standard deviation ranging from 1.6 to 13%. The achieved values were normalized by the value observed for graphite.

Solid-state nuclear magnetic resonance (NMR) spectra were recorded on an Agilent DD2 500WB spectrometer (11.7 T) with a resonance frequency of 125.70 MHz for ^{13}C. ^{13}C cross-polarization spectra were acquired in a 1.6 mm zirconia rotor and were spun at 15 kHz MAS rate. After a p/2 pulse of 2.5 ms on ^{1}H, the RF of ^{1}H was ramped from 79 to 100 kHz while the RF on ^{13}C was kept constant at 73.5 kHz during a contact time of 5 ms (spinning sideband condition). 100 kHz spinal-64 decoupling was applied on ^{1}H during acquisition. Recycle delays were set to 2.5 s and 8200 to 24000 scans were recorded depending on the sample.

Continuous-wave electron paramagnetic resonance (CW-EPR) spectra were recorded at room temperature using a Bruker ELEXSYS E500 spectrometer operating at X-band. Microwave power and amplitude modulation were respectively set to 1 mW and 1 G. Quantification of radical content was achieved using the Bruker weak-pitch standard sample (containing 1.29 10^{13} spin g^{-1}). The spin concentration is calculated from the double integration of the first derivative of the EPR signal. Pulsed-EPR experiments were carried out at 5 K using a

CoolEdge cryofree cryostat system. 2D Hyperfine Sublevel Correlation (HYSCORE) method was used for detecting ^{1}H, ^{13}C and ^{29}Si nuclei. The following pulse scheme was used $\pi/2-\tau-\pi/2-t_1-\pi-t_2-\pi/2-\tau$ echo and a four-step phase cycling where the echo is measured as a function of t_1 and t_2, with t_1 and t_2 being incremented by steps of 16 ns from their initial values. An optimum t value of 136 ns was used [19].

2.5 *In situ* GC experiment

The setup used for the synthesis of the hybrid materials was connected to a 7890A GC (Agilent Technologies (Santa Clara, CA, USA) gas chromatograph equipped with a FID detector and a CP-Sil PONA CB column (100 m × 0.25 mm × 0.5 µm), which allowed to monitor the ethylene conversion, and to a TCD connected to a J&W CP81071 column (1.5 m × 3.175 mm × 2 mm), which permitted to detect H_2 formation. The ethylene conversion was calculated without internal standard but directly from the area of the GC peaks using the equation 3 where $S_{ethylene_t}$ corresponds to the ethylene area at time *t* and $S_{ethylene_{BE}}$ to the ethylene area before the experiment.

$$\%C_{ethylene} = \frac{1-S_{ethylene_t}}{S_{ethylene_{BE}}} \times 100 \qquad (3)$$

The amount of substance corresponding to H_2 formation was obtained after carrying out a calibration curve. For the calibration curve, four experiments with different vol% of H_2 in a constant total flow rate allowed to determine the area of H_2 (supplementary information, **Table S1**, **Figure S9**).

3. Results and discussion

3.1 Characterization of the zeolite template

The beta zeolite that was used as template features a type I nitrogen adsorption isotherm at 77 K characteristic for microporous materials (**Figure S2a**). A typical micropore volume of 0.23 $cm^3\ g^{-1}$ was calculated [20]. The XRD powder pattern presents typical reflections of beta zeolites consisting of a mixture of different polymorphs (**Figure S2b**) [21]. The zeolite presents truncated bipyramidal morphology of polycrystalline nature with a particle size of approximately 5 µm (**Figure S3**). A global Si/Al ratio of 7.3 and a Brønsted acid site concentration of 600 µmol g^{-1} were measured (**Figure S4**). The thermal stability of the zeolite was confirmed by TGA and XRD (**Figure S5**).

3.2 Evolution of hybrid materials

3.2.1 Textural characterization of hybrid materials

Constant evolution of the textural properties during synthesis can be observed from the nitrogen physisorption isotherms at 77 K for the hybrid materials (**Figure 1a**). A rapid decrease of the micropore volume is remarked during the first 60 minutes of synthesis with a rate of 0.0024 $cm^3\ g^{-1}\ min^{-1}$ (**Figure 1b**). The reduction of micropore volume thereafter remains linear, yet slower (0.0012 $cm^3\ g^{-1}\ min^{-1}$). Complete filling of the micropores is achieved at 150 min (extrapolated value), indicating progressive development of carbon species during the first hour of synthesis. The reduction of the micropore filling rate thereafter might be related to diffusion constraints of ethylene within the micropore systems, as previously insinuated by Liu *et al.* [16]. Similar can be deduced from the NLDFT pore size distribution, which is centered at 6.4 Å during the first 60 minutes of synthesis (**Figure 1c**), indicating that microporosity is homogeneously filled during the first hour. Pore size distribution thereafter widens until complete loss of microporosity, suggesting a heterogeneous filling process probably related to diffusion issues.

3.2.2 Chemical and electrical characterization of hybrid materials

The structural packing density (SPD) increases progressively throughout the synthesis and reaches a maximum value of 0.29 g_C g_Z^{-1} after 240 min (**Figure 2a**). As expected, the evolution of the SPD is linear with the reduction of the zeolite micropore volume (**Figure S6**), indicating that the entirety of the carbonaceous species develops within the zeolite microporosity.

The apparent density of the carbonaceous species increases strongly and achieves a plateau within 60 min of synthesis at 1.12 g_C cm^{-3}, corresponding to approximately 60% of the maximum SPD (**Figure 2a**). The rapid progress of the apparent density during the first hour of synthesis indicates the important structural evolution of the carbonaceous species that develop within the zeolite microporosity. Apparent density remains constant thereafter, indicating consistent growth of carbon species.

It is interesting to note that the maximal combustion temperature is constant for hybrids obtained during the first 45 min of synthesis (560 °C), before progressively increasing to reach 610 °C for the hybrid achieved after heat treatment (**Figure 2b**). This suggests the development of smaller and individual polyaromatic molecules during the first 45 minutes of synthesis. The increase of the combustion temperature after 45 min indicates the growth of these species (**Figure 2b**). Shtein *et al.* [22] indeed reported the linear dependence of combustion temperature as a function of the size of condensed polyaromatic units.

The hybrid materials are electrical insulators during the first hour of synthesis, only thereafter electrical conductivity is detected (**Figure 2c**). The absence of electrical conductivity in hybrid samples fosters the suspicion of individual polyaromatic species that develop in the initial stages of the synthesis. The increase of the value of electrical conductivity thereafter

indicates the development of sp^2 conjugated carbon entities through the entire micropore system of the insulating zeolite crystals. This evidences condensation of polyaromatic hydrocarbons (PAHs) after the first hour of synthesis. Electrical conductivity significantly increases as a result of heat treatment. The heat treatment hence reveals as a key step for full condensation of the carbon skeleton.

The presence of PAHs could be detected through observing the Raman shift region between 400 and 900 cm^{-1} recorded at 532 nm (**Figure 3a**). It is important to recall that graphene does not exhibit any bands in this region, as well as for final carbon materials achieved during this study (**Figure 13a**). The features in this region can be ascribed to ring breathing modes and out-of-plane CH or CCC deformation modes of small PAH molecules (**Figure S7**). Cloutis *et al.* [23], revealed that the CCC deformation mode is very sensitive to p-electron density and occurs at lower Raman shifts for naphthalene and anthracene than for phenanthrene and pyrene. The confinement of PAHs in zeolites might further hinder or limit some vibration modes (especially the aromatic C-H deformation), which could lead to the displacement of the corresponding band positions [24]. The presence of various bands in this Raman shift region indicates the subsistence of a great variety of PAHs. The maximal intensity of the band centered at 590 cm^{-1} is reached when the zeolite micropore volume is completely occupied (**Figure 3b**). The decrease of I_{590} value after 180 min and notably upon heat treatment suggests condensation of PAHs, indicating a more connected carbon network.

Raman spectra excited at 266 and 532 nm further present intense and large contributions between 1100 and 1700 cm^{-1} (**Figure 3c and S8**). The G band represents the vibrational mode associated with asymmetric stretching of the entirety of sp^2 carbon atoms, whereas the D band is attributed to the breathing mode in aromatic rings of PAHs [25-27]. The G band position remains constant at approximately 1610 cm^{-1} during the first hour of synthesis, which suggests fast nucleation to form higher condensed PAHs. Indeed, small linear PAHs, such as

naphthalene or anthracene present G bands typically centered at higher wavenumbers (1633 cm^{-1}), while higher condensed PAHs, such as chrysene or pyrene appear at lower shifts (1605-1617 cm^{-1}) [28]. After 1 h of synthesis the position of the G bands redshifts down to 1597 cm^{-1} (**Figure 3d**). This downshift is attributed to the higher delocalization of π electrons [26,27], which suggests the beginning of condensation of the carbon network. As far as the D band position is concerned, a constant redshift is observed throughout the first 120 min of synthesis from 1420 to 1375 cm^{-1}, indicating the steady growth of PAHs [25,29]. The achievement of a plateau after 120 min of synthesis of the D band position indicates no further growth of PAHs thereafter (**Figure 3e**). This corresponds to the complete filling of zeolite microporosity.

It is important to further note that the G band reaches the lowest position at 1597 cm^{-1}. This value is higher to what is typically observed for nano-graphene domains or microcrystalline graphite-like materials [31-34]. Likewise, the D band reaches a position that is higher than the value typically recorded for nano-graphene (i.e. 1360 cm^{-1}). This hence strongly indicates that the assignment of ZTCs as 3D graphenes could be erroneous [2]. The G and D bands hence rather result from individual and condensed PAHs, which might be considered as precursors of nano-sized graphitic clusters [29,35,36].

The intensity of Raman bands (achieved by normalization on the intratetrahedral OTO zeolite bending band at 420 cm^{-1} for spectra recorded at 266 nm) develop steadily but rather slowly during the first 120 min of synthesis, followed by a stronger and linear increase of the intensities (**Figure 3f**). It is known that with increasing number of condensed rings the band intensities increase importantly in D_{2h} PAHs, such as in rylenes [37]. For large 2-dimensional D_{3h} PAHs, the D band intensity is significantly higher than the G band [29]. In our case the intensity ratio between the D and the G band is closer to that observed for PAHs featuring pseudo one-dimensional D_{2h} point symmetry, such as for rylenes or carbon nanoribbons. The large PAHs formed in the zeolite channels hence present an elongated shape along the axis of

the channels. Moreover, D_{2h} PAHs typically present a shoulder next to the D band (around 1200 cm^{-1}) [37]. It is interesting to note that a similar shoulder is observed for the hybrid materials achieved in the present work (**Figure 3c and S8**). The position of the S band redshifts with increasing synthesis time, which indicates that the length of the D_{2h} PAHs increases during the ZTC formation through growth and condensation [38].

The Raman spectra further allow for observing stretching bands at 2775 and 2952 cm^{-1}, which indicate that the PAH species are alkylated. The presence of such alkyl chains further leads to Raman features between 1100 - 1460 cm^{-1} resulting from CH_2 or CH_3 deformation modes, which yet overlap with the wide S, D and G bands.

To achieve further insights into the development of the carbon species, the hybrid materials were characterized with EPR spectroscopy. The CW-EPR spectra allow for the unprecedented observation of the radical nature of the hybrid samples (**Figure 4**). The spin concentration is a function of the SPD and increases from 1.8 to 16.1 spin g^{-1} for 5 and 240 min+HT, respectively (**Figure 4b**). The radicals in the hybrid materials are stable as no substantial decrease in spin concentration was detected after 14 months of storage at RT (**Figure S11**).

The hybrid materials display a single line centered at a g factor of 2.0038 on EPR spectra (**Figure 4a**). The linewidth evolves with synthesis time and increases from 5.2 to 12 G and from Lorentzian to stretched Lorentzian for the hybrid materials achieved after 5 min and 240min+HT, respectively. It is known that the linewidth is impacted by the clustering of spins, and is typically of Lorentzian shape and narrow for amorphous carbon-based materials [39]. Broadening of the linewidth indicates random uniform spin concentration due to the spin-spin dipolar broadening relation [40]. Tabbal *et al.* observed increasing linewidth with a growing degree of the connectivity of sp^2 domains in carbon films [41]. The development of the linewidth here hence indicates the evolution from a clustered to a homogeneous spin

system, which is coherent to the observation of individual PAH formation in the initial stages of the synthesis, which then further grow and further condense.

The observation of the development of radical PAH species in zeolites can be related to what is known from coke formation during catalytic deactivation of zeolites [42]. Coke is a mixture of PAH molecules, which structure depends on the zeolite framework and reaction temperature. For beta zeolite coke species that develop in hydrocarbon transformation at 450 °C consist of a large mixture of PAH molecules with an oblong shape in the channel directions [43,44]. Coke molecules based on naphthalene, anthracene, cyclopentapyrene, etc. could be extracted from zeolite beta as soluble coke fraction and present important radical character due to the spontaneous charge separation as a function of the framework [19,45,46]. Elongated large PAH species are thus certainly formed in the initial stages of the ZTC synthesis through aromatization and growth (**Scheme 1**). The presence of acid site catalysis plays a crucial role in these reactions. Zeolite acidity hence seems required for the development of ZTCs. Indeed, an experiment using all-silica beta zeolite did not allow for the formation of carbonaceous compounds in the zeolite microporosity using the same synthesis conditions (**Figure S10**).

To gather further insights into the structure and the nature of the radical species pulsed EPR experiments were performed. The 2D-HYSCORE spectra represent the correlation between the nuclear frequencies of the spin states (up and down) of the electron and give the nuclear frequencies and the hyperfine interactions of nuclei in the vicinity of the unpaired electron spin [47]. The 2D-HYSCORE method hence enables the assignment of couplings of a large number of nuclei, such as ^{1}H, ^{13}C and ^{29}Si. ^{1}H and ^{13}C signals were observed at typical Larmor frequencies of 14.5 and 3.7 MHz (**Figure 5**).

Table 1. $^{13}C/^{1}H$ ratio in hybrid and carbon materials at selected syntheses times.

Synthesis time (min)	$^{13}C/^{1}H$ in hybrid materials	$^{13}C/^{1}H$ in carbon materials
5	0.72	0.033
30	0.89	0.88
60	0.43	0.58
240	0.47	0.69

From the shape of the ^{1}H-HYSCORE signal (14.5 MHz) important conclusions on the nature of the C-H bonds in radical samples can be drawn. Typical features of radicals composed of a polyaromatic core terminated either by hydrogens or branched aliphatic chains can be deduced. The ^{1}H-HYSCORE signal becomes larger with increasing synthesis time. The growth of the dipolar part with synthesis time suggests increasing number of aromatic hydrogens, due to shorter electron-nucleus distances [19]. This observation hence allows to conclude the increase in the number of condensed aromatic cycles with synthesis time. As all samples were recorded with the same τ value of 136 ns and as t_1 (540µs) and t_2 (2µs), the $^{13}C/^{1}H$ ratio could be measured (**Table 1**). The $^{13}C/^{1}H$ ratio grows slightly during the first 30 min before decreasing with increasing synthesis time. $^{13}C/^{1}H$ ratios are typically greater for polyaromatic samples containing a higher degree of aliphatic branchings, as carbon atoms located at short distances from the polyaromatic unit increase the probability for unpaired electrons to interact with ^{13}C nuclei [48]. $^{13}C/^{1}H$ ratios can hence not be compared to molar C/H ratios detected by other techniques, such as elemental analysis. The decrease in $^{13}C/^{1}H$ ratio hence indicates that the degree of aliphatic moieties increases during the first 30 min of synthesis before reducing probably as a result of PAHs growth.

For the sample at 30 min and at higher syntheses times a ^{29}Si Larmor frequency signal (2.9 MHz) along the diagonal is observed, from which no structural information can be drawn. The presence of this signal yet allows to foster the hypothesis that radicals develop through spontaneous ionization of the developing carbon species in the zeolite microporosity.

3.2.3 In situ *observation of ethylene conversion and hydrogen production*

Figure 6 presents the *in situ* time resolved observation of the conversion of ethylene and the production of hydrogen. High ethylene conversion is observed at the beginning of the synthesis (11%), which rapidly decreases during the first hour (2.5%). A rate change in ethylene conversion is observed after the first hour of synthesis, which indicates a regime change in the reaction (from kinetic to diffusional), and confirms to what was previously deduced from nitrogen physisorption, TGA and Raman spectroscopy. The carbon mass balance was established by taking into account the SPD, which allows to calculate that approximately 38 mol% of the converted can be found in the final ZTC. The remaining ethylene is hence converted into smaller aromatic and aliphatic molecules within the zeolite with a mean C/H ratio of 0.35, which diffuse out of the micropore system during the ZTC synthesis.

Hydrogen production is highest at the beginning of the synthesis and then follows a similar trend as the ethylene conversion during the 4 h of ethylene feeding, yet without dropping completely to zero (**Figure 6b**). During the subsequent heat treatment step hydrogen production increases slightly, indicating further reaction of the carbon species (condensation) within the zeolite porosity. This hydrogen production further explains the slight reduction of the SPD of the hybrids during the heat treatment step (**Figure 2a**).

3.3 Evolution of the carbon materials

3.3.1 Textural, morphological and structural characterization of carbon materials

The nitrogen physisorption isotherms of the carbon materials allow to deduce the evolution of the textural properties as a function of the synthesis time (**Figure 7**). Nitrogen volume for adsorption and desorption for a relative pressure of 0.43 do not match (open hysteresis loop) for all carbons, except for the material achieved after heat treatment (**Figure 7a**). Open hysteresis loops are classically observed for not fully cross-linked polymers and can be ascribed to deformation/swelling of the network during adsorption [49], and hence indicates that the carbon backbone is not fully condensed even after complete micropore filling of the zeolite. Only after the heat treatment step the desorption branch closes the adsorption branch at P/P_0 = 0.43, indicating that the material is fully connected as a result of the high temperature treatment. This observation thus confirms what was observed from the electrical conductivity measurements on the hybrid materials.

The microporosity develops in three stages: (*i*) linear evolution up to 60 min of synthesis with no clear micropore size distribution. This suggests that the carbons achieved during the first hour do not present any textural features that can be related to the zeolite structure (**Figure 7b**). (*ii*) Steady increase during the further three hours of synthesis of micropore volume and narrowing of the micropore size distribution. First textural features from zeolite templating hence become observable after 1 h of synthesis. (*iii*) High increase of micropore volume (+40%) with further narrowing of pore size distribution as a result of the heat treatment step.

XRD powder patterns were recorded as high quality ZTCs allow for the observation of reflections related to structural long range order [11]. The carbon materials achieved after short syntheses times (below 60 min) do not present any XRD peaks related to the structural order of ZTCs but a broad reflection centered at 24° 2θ can be observed (**Figure 8**). This latter can be ascribed to the (002) reflection, resulting from the stacking of graphene-like subunits, typically observed in unstructured carbons as in activated carbons [50]. The

presence of the (002) reflection hence indicates that unstructured carbon materials are achieved after zeolite dissolution during the first hour of synthesis.

The characteristic carbon stacking reflection (002) disappears in XRD powder patterns after 60 min and a peak at 7.6° 2θ begins to emerge (**Figure 8**), indicating the beginning of partial long range order in the carbon materials, characteristic for ZTCs. Upon heat treatment a further peak at 15.0° 2θ, which is characteristic for ZTCs resulting from beta zeolite featuring high structural quality [11].

The results achieved from nitrogen physisorption and XRD are confirmed by electron microscopy images. SEM images present unstructured and large carbon agglomerates of undefined morphology achieved for the carbon materials at short syntheses times that do not result from zeolite templating (**Figure 9**). Only for carbons achieved after 1 h of synthesis typical morphological features of the zeolite shape start to emerge. Similar is inferred from the TEM images. Structured microporosity allowing for electron diffraction peaks is only observed after the heat treatment step (**Figure 10**).

3.3.2 Chemical characterization of carbon materials

Nitrogen physisorption, XRD patterns and electron microscopy images suggest that unstructured carbons are achieved during the first hour of synthesis. From the characterization of the hybrid materials the presence of individual PAHs was evidenced at short (< 60 min) syntheses times. Yet, an attempt to extract soluble polyaromatic molecules through zeolite dissolution did not result successful as surprisingly only insoluble carbon residues were obtained, even for very short syntheses times (5 min). This fosters the hypothesis that individual PAHs react together upon zeolite dissolution, which might be related to the radical nature of the carbon species in the hybrid material.

It is further interesting to note that the carbon materials extracted during the first hour of synthesis still present an important spin concentration, probably due to the fast and uncontrolled reaction of the PAHs upon zeolite dissolution, leading hence to carbons that present persistent radicals (**Figure 11**). Such permanent radicals have been described for biochars and hydrochars [51]. It is conspicuous that carbon materials after heat treatment do not present any spin concentration, which might result from radical quenching of fully condensed carbon skeletons. It is interesting to note that the presence of unpaired electron spins has previously been reported by Kyotani and co-workers for ZTCs, which might result from the use of acetylene as carbon precursor [52-54].

The linewidth of CW-EPR spectra increases from 4 to 7 G from 30 to 240 min, respectively (**Figure 11b**). As for the hybrid materials, the broadening of the linewidth indicates a higher degree of connectivity of sp^2 domains. 2D-HYSCORE patterns present similar features as for the hybrid materials except for the $^{13}C/^{1}H$ ratio (**Table 1** and **Figure 12**). A very low ratio (0.033) is achieved for the sample after 5 min of synthesis indicating the development of highly clustered radical species in the beginning. Thereafter, values are similar to those observed for the hybrid materials. This indicates that the sample achieved after 5 min is strongly modified during the dissolution process.

The Raman spectra recorded at 532 nm of the carbon materials feature important differences compared to those of the hybrid materials (**Figure 13**). The most striking difference is the absence of features in the low Raman shift region (400 – 900 cm^{-1}) for all of the carbon samples, which fosters the hypothesis that individual PAHs react together during dissolution of the zeolite. Moreover, the positions of the G and D bands remain rather constant for all hybrid materials independently of the synthesis time, indicating that caution needs to be taken when interpreting the quality of ZTCs from Raman spectra alone.

The C/H ratio evolves steadily from 2.5 to 3.5 during the entire synthesis (**Figure 14a**). This suggest progressive growth of PAHs toward the formation of the condensed ZTC skeleton. To further study the chemical nature of samples ^{13}C solid-state NMR spectra were recorded under magic angle spinning with the cross polarization (CP) technique for hybrid and carbon materials after 240 min+HT (**Figure 14b**). In both spectra, three contributions of aromatic carbon atoms can be discerned and decomposed. They are attributed to two types of aromatic *C*-H carbon atoms (123 and 128 ppm) and to quaternary carbon atoms in extended aromatic systems (138 ppm) [55]. It is to note that the resonances are very broad in the hybrid material, but narrower in the final carbon material, which can be related to the absence of radicals in the final carbon material after heat treatment (**Figure 14b**). Note that in CP MAS NMR spectra, the signal intensity relies on polarization transfer from nearby protons to heteronuclei, here ^{13}C, and therefore, the intensity of the quaternary carbon resonances may be underestimated.

The carbon materials further present a scant amount of oxygen with an overall C/O ratio of 12 to 13 (**Figure 14a**). The presence of oxygen was previously ascribed either as resulting from the reaction of the forming carbon network with the oxygen atoms of the zeolite framework [16], or more often from the zeolite dissolution process [56]. In the ^{13}C NMR spectrum of the carbon, a further contribution at 180 ppm is indeed distinguishable, which can be ascribed to carbonyl or carboxylic groups and demonstrates the incorporation of oxygen into the network during the zeolite dissolution treatment. The absence of other signals, in particular the absence of signals around 160 ppm, excludes the presence of aromatic alcohols or aromatic C-F bonds. We hence hypothesize that radical species in the hybrid material react with water molecules during zeolite dissolution, which may explain the presence of oxygen in the carbon materials.

5. Conclusion

New insights into the ZTCs formation process were obtained by studying both the formation of the hybrid materials and carbons at different syntheses times. Chemical, structural, electrical, textural and morphological characterization of the achieved materials allowed us to conclude that the ZTC formation occurs in three major stages, which can be ascribed to nucleation, growth and condensation:

Stage I: PAHs develop through aromatization of ethylene and growth, catalyzed through the acid sites of the zeolites. Oblong, rylene-type PAHs preferentially develop in the extended micropore channels of beta zeolite. The PAHs are of radical nature and react together upon zeolite dissolution, leading to unstructured carbon particles of undefined morphology and random textural properties, which present permanent radical character. This stage was observed for syntheses times below 1 h in the applied conditions.

Stage II: Typical structural, textural and morphological features of ZTCs start to emerge. Increased connectivity of the individual PAHs is evidenced through partial electrical conductivity of hybrid materials. The achieved carbon materials can be described as composites of ZTC and randomly reacted PAHs molecules. This stage was firstly observed after 60 min of synthesis.

Stage III: Heat treatment triggers the final condensation of the ZTC network. Textural, morphological, structural, and electrical features develop which result from the zeolite templating. Final ZTCs feature carbonyl or carboxyl functionalization, which is inherent to the zeolite dissolution step and results probably from radical quenching with water.

The disclosed findings allow for firstly presenting a reaction mechanism of the ZTC formation. Beyond a pure kinetic study on zeolite mass gain during ZTC synthesis, the

present study allows to conclude that ZTC synthesis occurs through the nucleation and growth of individual hydrocarbon species. The classical description of ZTC synthesis as CVD process or as “carbon deposition process” must hence be revised. We can further stipulate that ZTC formation riles on a dynamic and complex mechanism in which the chemical properties of the zeolite play a crucial role on the chemical and structural properties of the resulting carbon material. The thorough characterization of the hybrid materials (zeolite/carbon) further allowed us to query on the possible role of radical species in the condensation of the final ZTC upon zeolite dissolution. This latter assumption remains to be verified.

The now common description of ZTCs as nanographenes needs further to be revised. From the results that the present study offers the properties of ZTCs formed in beta zeolite rather resemble to a network of connected polyaromatic hydrocarbons, which most probably feature heterogeneous structural properties.

Supporting Information

Further characterization of the zeolite template, hybrid and carbon materials are available as supporting information.

ACKNOWLEDGMENTS

T.A., I.B., Y.P., L.P. and A.S. acknowledge financial support from the European Union (ERDF) and "Région Nouvelle Aquitaine". D.W. thanks the Cluster of Excellence Engineering of Advanced Materials for funding (Starting Grant EAM-SG20-2).

References

[1] H. Nishihara, T. Kyotani, Zeolite-templated carbons – three-dimensional microporous graphene frameworks, Chem. Commun. 54 (2018) 5648-5673. https://doi.org/10.1039/C8CC01932K.

[2] T. Kyotani, T. Nagai, S. Inoue, A. Tomita, Formation of New Type of Porous Carbon by Carbonization in Zeolite Nanochannels, Chem. Mater. 9 (1997) 609-615. https://doi.org/10.1021/cm960430h.

[3] F. Su, X. S. Zhao, L. Lv, Z. Zhou, Synthesis and characterization of microporous carbons templated by ammonium-form zeolite Y, Carbon 42 (2004) 2821-2831. https://doi.org/10.1016/j.carbon.2004.06.028.

[4] C. J. Meyers, S. D. Shah, S. C. Patel, R. M. Sneeringer, C. A. Bessel, N. R. Dollahon, R. A. Leising, E. S. Takeuchi, Templated Synthesis of Carbon Materials from Zeolites (Y, Beta, and ZSM-5) and a Montmorillonite Clay (K10): Physical and Electrochemical Characterization, J. Phys. Chem. B 105 (2001) 2143-2152. https://doi.org/10.1021/jp0029663.

[5] Z. Ma, T. Kyotani, Z. Liu, O. Terasaki, A. Tomita, Very High Surface Area Microporous Carbon with a Three-Dimensional Nano-Array Structure: Synthesis and Its Molecular Structure, Chem. Mater. 13 (2001) 4113-4415. https://doi.org/10.1021/cm010730l.

[6] E. Braun, Y. Lee, M. Moosavi, S. Barthel, R. Mercado, I.A. Baburin, D.M. Proserpio, B. Smit, Generating carbon schwarzites via zeolite-templating, PNAS 115 (2018) E8116. https://doi.org/10.1073/pnas.1805062115.

[7] E.E. Taylor, K. Garman, N.P. Stadie, Atomistic Structures of Zeolite-Templated Carbon, Chem. Mater. 32 (2020) 2742–2752. https://doi.org/10.1021/acs.chemmater.0c00535.

[8] T. Lee, S. H. Ko, S.J. Cho, R. Ryoo, Ultramicroporous Carbon Synthesis Using Lithium-Ion Effect in ZSM-5 Zeolite Template, Chem. Mater. 30 (2018) 6513–6520. https://doi.org/10.1021/acs.chemmater.8b03132.

[9] S. Lei, J. Miyamoto, T. Ohba, H. Kanoh, K. Kaneko, Novel Nanostructures of Porous Carbon Synthesized with Zeolite LTA-Template and Methanol, J. Phys. Chem. C 111 (2007) 2459–2464. https://doi.org/10.1021/jp066564s.

[10] E. F. Oliveira, L. D. Machado, R.H. Baughman, D. S. Galvao, Three-dimensional carbon nanotube networks from beta zeolite templates: Thermal stability and mechanical properties, Comput. Mater. Sci. 182 (2020) 109781. https://doi.org/10.1016/j.commatsci.2020.109781.

[11] T. Aumond, M. Esteves, Y. Pouilloux, R. Faccio, A. Sachse, Impact of the crystal size of beta zeolite on the structural quality of zeolite templated carbons, Microporous Mesoporous Mater. 331 (2022) 111644. https://doi.org/10.1016/j.micromeso.2021.111644.

[12] G. Yang, L. Li, H. Liu, Y. Cheng, Y. Chen, X. Li, Metal ion (Ca2+, Mg2+, Zn2+) catalyzed synthesis of high-quality zeolite templated carbon, Microporous Mesoporous Mater. 336 (2022) 111860. https://doi.org/10.1016/j.micromeso.2022.111860.

[13] A. Garsuch, O. Klepel, R.R. Sattler, C. Berger, R. Gläser, J. Weitkamp, Synthesis of a carbon replica of zeolite Y with large crystallite size, Carbon 44 (2006) 593-596. https://doi.org/10.1016/j.carbon.2005.10.005.

[14] J. Parmentier, V. Valtchev, F. Gaslain, L. Tosheva, C. Ducrot-Boisgontier, J. Moller, J. Patarin, C. Vix-Guterl, Effect of the zeolite crystal size on the structure and properties of carbon replicas made by a nanocasting process, Carbon 47 (2009) 1066-1073. https://doi.org/10.1016/j.carbon.2008.12.030.

[15] T. Aumond, J. Rousseau, Y. Pouilloux, L. Pinard, A. Sachse, Synthesis of hierarchical zeolite templated carbons, Carbon Trends 2 (2021) 100014. https://doi.org/10.1016/j.cartre.2020.100014.

[16] Y. Liu, J. Wang, M.A. Serageldin, T. Wang, W.-P. Pan, Carbon deposition mechanism and structural changes for zeolite-templated carbons, Microporous Mesoporous Mater. 324 (2021) 111311. https://doi.org/10.1016/j.micromeso.2021.111311.

[17] H. Nishihara, K. Imai, H. Itoi, K. Nomura, K. Takai, T. Kyotani, Formation mechanism of zeolite-templated carbons, TANSO 280 (2017) 169-174. https://doi.org/10.7209/tanso.2017.169.

[18] M.A. Camblor, A. Corma, S. Valencia, Synthesis in fluoride media and characterisation of aluminosilicate zeolite beta, J. Mater. Chem. 8 (1998) 2137–2145. https://doi.org/10.1039/A804457K.

[19] K.B. Tayeb, S. Hamieh, C. Canaff, H. Nguyen, H. Vezin, L. Pinard, The radical internal coke structure as a fingerprint of the zeolite framework, Microporous Mesoporous Mater. 289 (2019) 109617. https://doi.org/10.1016/j.micromeso.2019.109617.

[20] M.A. Camblor, A. Corma, S. Valencia, Characterization of nanocrystalline zeolite Beta, Microporous Mesoporous Mater. 25 (1998) 59–74. https://doi.org/10.1016/S1387-1811(98)00172-3.

[21] T. Lu, W. Yan, R. Xu, Chiral zeolite beta: structure, synthesis, and application, Inorg. Chem. Front. 6 (2019) 1938-1951. https://doi.org/10.1039/C9QI00574A.

[22] M. Shtein, I. Pri-Bar, M. Varenik, O. Regev, Characterization of Graphene-Nanoplatelets Structure via Thermogravimetry, Anal. Chem. 87 (2015) 4076–4080. https://doi.org/10.1021/acs.analchem.5b00228.

[23] E. Cloutis, P. Szymanski, D. Applin, D. Goltz, Identification and discrimination of polycyclic aromatic hydrocarbons using Raman spectroscopy, Identification and discrimination of polycyclic aromatic hydrocarbons using Raman spectroscopy, Icarus 274 (2016) 211-230. https://doi.org/10.1016/j.icarus.2016.03.023.

[24] G. Socrates, Infrared and Raman Characteristic Group Frequencies, Third edition, John Wiley and Sons, (2004) ISBN: 978-0-470-09307-8.

[25] M.W. Smith, I. Dallmeyer, T.J. Johnson, C.S. Brauer, J.-S. McEwen, J.F. Esoinal, M. Garcia-Perez, Structural analysis of char by Raman spectroscopy: Improving band assignments through computational calculations from first principles, Carbon 100 (2016) 678-692. https://doi.org/10.1016/j.carbon.2016.01.031.

[26] J. Schwan, S. Ulrich, V. Batori, H. Ehrhardt, Raman spectroscopy on amorphous carbon films, J. Appl. Phys. 80 (1996) 440-447. https://doi.org/10.1063/1.362745.

[27] K.H. Michaelian, S.A. Oladepo, J.M. Shaw, X. Liu, D. Bégué, I. Baraille, Raman and photoacoustic infrared spectra of fluorene derivatives: Experiment and calculations, Vibrational Spectroscop. 74 (2014) 33-46. https://doi.org/10.1016/j.vibspec.2014.07.003.

[28] P.M. Allotta, P.C. Stair, Time-Resolved Studies if Ethylene and Propylene Reactions in Zeolite H-MFI bi In-Situ IR Heating and UV Raman Spectroscopy, ACS Catal. 2 (2012) 2424-2432. https://doi.org/10.1021/cs3004215.

[29] F. Negri, C. Castiglioni, M. Tommasini, G. Zerbi, A Computational Study of the Raman Spectra of Large Polycyclic Aromatic Hydrocarbons: Toward Molecularly Defined Subunits of Graphite, J. Phys. Chem. A 106 (2002) 3306-3317. https://doi.org/10.1021/jp0128473.

[30] S. Medina Rivero, S. Canola, W. Zeng, F. J. Ramírez, J. L. Zafra, J. Wu, F. Negri, J. Casado, Long rylene nanoribbons express polyacetylene-like signatures at their edges, Phys. Chem. Chem. Phys., 2019,21, 7281-7287. https://doi.org/10.1039/C9CP00679F.

[31] N. Shimodaira, A. Masui, Raman spectroscopic investigations of activated carbon materials, J. Appl. Phys. 92 (2002) 902-909. https://doi.org/10.1063/1.1487434.

[32] M.S. Dresselhaus, A. Jorio, R. Saito, Characterizing Graphene, Graphite, and Carbon Nanotubes by Raman Spectroscopy, Annu. Rev. Condens. Matter Phys. 1 (2010) 89-108. https://doi.org/10.1146/annurev-conmatphys-070909-103919

[33] C. Ferrari, Raman spectroscopy of graphene and graphite: Disorder, electron–phonon coupling, doping and nonadiabatic effects, Solid State Commun 143 (2007) 47-57. https://doi.org/10.1016/j.ssc.2007.03.052.

[34] A. C. Ferrari, J. Robertson, Interpretation of Raman spectra of disordered and amorphous carbon Phys. Rev. B 61 (2000) 14095-14107. https://doi.org/10.1103/PhysRevB.61.14095.

[35] L. Colangeli, V. Mennella, G.A. Baratta, E. Bussoletti, G. Strazzulla, Raman and infrared spectra of polycyclic aromatic hydrocarbon molecules of possible astrophysical interest, J. Astrophysics 396 (1992) 369-377. https://doi.org/10.1086/171723.

[36] Y. Tann Chua, P.C. Stair, An ultraviolet Raman spectroscopic study of coke formation in methanol to hydrocarbons conversion over zeolite H-MFI, J. Catal. 213 (2003) 39-46. https://doi.org/10.1016/S0021-9517(02)00026-X.

[37] M. Rigolio, C. Castiglioni, G. Zerbi, F. Negri, Density functional theory prediction of the vibrational spectra of polycyclic aromatic hydrocarbons: effect of molecular symmetry and size on Raman intensities, J. Mol. Struct. 563-364 (2001) 79-87. https://doi.org/10.1016/S0022-2860(00)00953-4.

[38] J. Kim, N. Lee, Y. H. Min, S. Noh, N.-K. Kim, S. Jung, M. Joo, Y. Yamada, Distinguishing Zigzag and Armchair Edges on Graphene Nanoribbons by X-ray Photoelectron and Raman Spectroscopies, ACS Omega, 12 (2018) 17789–17796. https://doi.org/10.1021/acsomega.8b02744.

[39] R.C. Barklie, Characterisation of defects in amorphous carbon by electron paramagnetic resonance, Diamond and Related Materials, 12 (2003) 1427-1434. https://doi.org/10.1016/S0925-9635(03)00004-9.

[40] R. C. Barklie, M. Collins, S. R. P. Silva, EPR linewidth variation, spin relaxation times, and exchange in amorphous hydrogenated carbon, Phys. Rev. B 61 (2000) 3546-3554. https://link.aps.org/doi/10.1103/PhysRevB.61.3546.

[41] M. Tabbal, T. Christidis, S. Isber, P. Mérel, M. A. El Khakani, M. Chaker, A. Amassian L. Martinu, Correlation between the sp2-phase nanostructure and the physical properties of unhydrogenated carbon nitride, Journal of Applied Physics 98 (2005) 044310. https://doi.org/10.1063/1.2009817.

[42] M. Guisnet, P. Magnoux, Organic Chemistry of coke formation, Appl. Catal. A 212 (2001) 83-96. https://doi.org/10.1016/S0926-860X(00)00845-0.

[43] L. Pinard, Hamieh, C. Canaff, F. Ferreira Madeira, I. Batonneua-Gener, S. Maury, O. Delpux, K. Ben Tayeb, Y. Pouilloux, H. Vezin, Growth mechanism of coke on HBEA zeolite during ethanol transformation, J. Catal. 299 (2013) 284-297. https://doi.org/10.1016/j.jcat.2012.12.018.

[44] P. Magnoux, A. Rabeharitsara, H. S. Cerqueira, Influence of reaction temperature and crystallite size on HBEA zeolite deactivation by coke, Apple. Catal. A 304 (2006) 142-151. https://doi.org/10.1016/j.apcata.2006.02.040.

[45] A. Moissette, F. Luchez, C. Bremard, H. Vezin, M. Hureau, Spontaneous charge separation induced by phenothiazinesorption within acidic H_nZSM-5, Phys. Chem. Chem. Phys. 11 (2009) 4286–4297. https://doi.org/10.1039/B900324J.

[46] T. Crémoux, I. Batonneau-Gener, A. Moissette, J.-L. Paillaud, M. Hureau, E. Ligner, C. Morais, S. Laforge, C. Marichal, H. Nouali, Influence of framework Si/Al ratio and topology on electron transfers in zeolites, Phys. Chem. Chem. Phys. 21 (2019) 14892-14903. https://doi.org/10.1039/C9CP01166H.

[47] P. Höfer, A. Grupp, H. Nebenführ, M. Mehring, Hyperfine sublevel correlation (hyscore) spectroscopy: a 2D ESR investigation of the squaric acid radical, Chem. Phys. Lett. 132 (1986) 279-282. https://doi.org/10.1016/0009-2614(86)80124-5.

[48] D. Gourier, O. Delpoux, L. Binet, H. Vezin, Nuclear Magnetic Biosignatures in the Carbonaceous Matter of Ancient Cherts: Comparison with Carbonaceous Meteorites, Astrobiology, 13 (2013) 932-947. https://doi.org/10.1089/ast.2013.0971.

[49] J. Weber, J. Schmidt, A. Thomas, W. Böhlmann, Micropore Analysis of Polymer Networks by Gas Sorption and 129Xe NMR Spectroscopy: Toward a Better Understanding of Intrinsic Microporosity, Langmuir, 26 (2010) 15650-15656. https://doi.org/10.1021/la1028806.

[50] B. Qi, L. Di, W. Xu, X. Zhang, Dry plasma reduction to prepare a high performance Pd/C catalyst at atmospheric pressure for CO oxidation, J. Mater. Chem. A 2 (2014) 11885. https://doi.org/10.1039/C4TA02155J.

[51] Y. Qin, G. Li, Y. Gao, L. Zhang, Y.S. Ok, T. An, Persistent free radicals in carbon-based materials on transformation of refractory organic contaminants (ROCs) in water: A critical review, Water Res. 137 (2018) 130-143. https://doi.org/10.1016/j.watres.2018.03.012.

[52] K. Takai, T. Suzuki, T. Enoki, H. Nishihara, T. Kyotani, Fabrication and characterization of magnetic nanoporous zeolite templated carbon, J. Phys. Chem. Solids 71 (2010) 565-568. https://doi.org/10.1016/j.jpcs.2009.12.037.

[53] K. Takai, T. Suzuki, T. Enoki, H. Nishihara, T. Kyotani, Structure and magnetic properties of curved graphene networks and the effects of bromine and potassium adsorption, Phys. Rev. B 81 (2010) 205420. https://doi.org/10.1103/PhysRevB.81.205420.

[54] A. Gabe, M. Ouzzine, E. E. Taylor, N. P. Stadie, N. Uchiyama, T. Kanai, Y. Nishina, H. Tanaka, Z.-Z. Pan, T. Kyotani, H. Nishihara, High-density monolithic pellets of double-sided graphene fragments based on zeolite-templated carbon, J. Mater. Chem. A 9 (2021) 7503-7507. https://doi.org/10.1039/D0TA11625D.

[55] N.J. Brownbill, R. Sebastian Sprick, B. Bonillo, S. Pawsey, F. Aussenac, A. J. Fielding, A. I. Cooper, F. Blanc, Structural Elucidation of Amorphous Photocatalytic Polymers from Dynamic Nuclear Polarization Enhanced Solid State NMR, Macromolecules 51 (2018) 3088–3096. https://doi.org/10.1021/acs.macromol.7b02544.

[56] H. Park, S. K. Terhorst, R. Kumar Bera, R. Ryoo, Template dissolution with NaOH–HCl in the synthesis of zeolite-templated carbons: Effects on oxygen functionalization and electrical energy storage characteristics, Carbon 115 (2019) 570-579. https://doi.org/10.1016/j.carbon.2019.09.020.

[57] D. Massiot, F. Fayon, M. Capron, I. King, S. Le Calvé, B. Alonso, J.-O. Durand, B. Bujoli, Z. Gan, G. Hoatson, Modelling one- and two-dimensional solid-state NMR spectra, Mag. Reson. Chem. 40 (2002) 70-76. https://doi.org/ 10.1002/mrc.984.

Figures

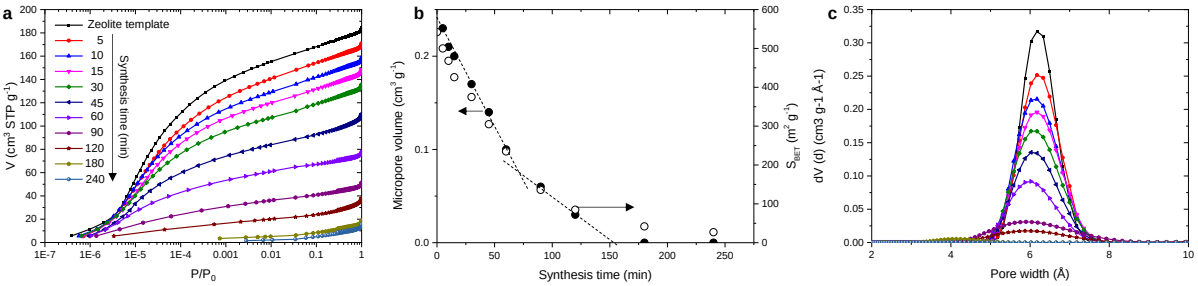

Figure 1. a) Nitrogen physisorption isotherms at 77 K of hybrid materials achieved at different syntheses times. b) Evolution of the micropore volume and of the BET surface area of the hybrid materials as a function of the synthesis time. c) NLDFT pore size distribution based on nitrogen physisorption isotherms at 77 K of hybrid materials.

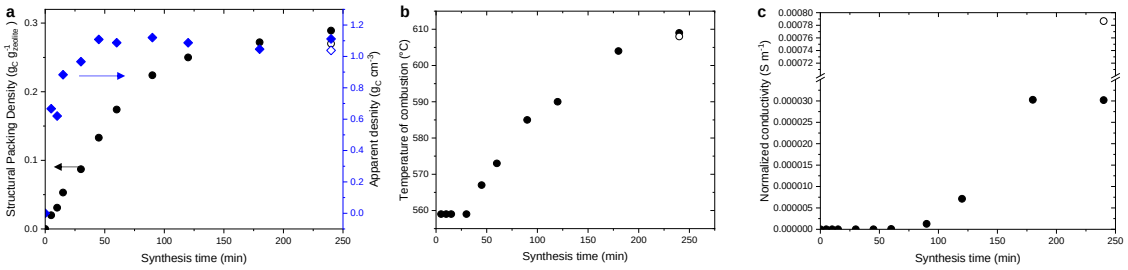

Figure 2. Evolution of the structural packing density (SPD, black circles) and apparent density (blue diamonds) as a function of the synthesis time for hybrid compounds (a). Evolution of the maximal temperature of combustion as a function of the synthesis time for hybrid compounds (b). Evolution of normalized electronic conductivity of hybrids as a function of synthesis time (c). Empty symbols correspond to the sample 240 min+HT.

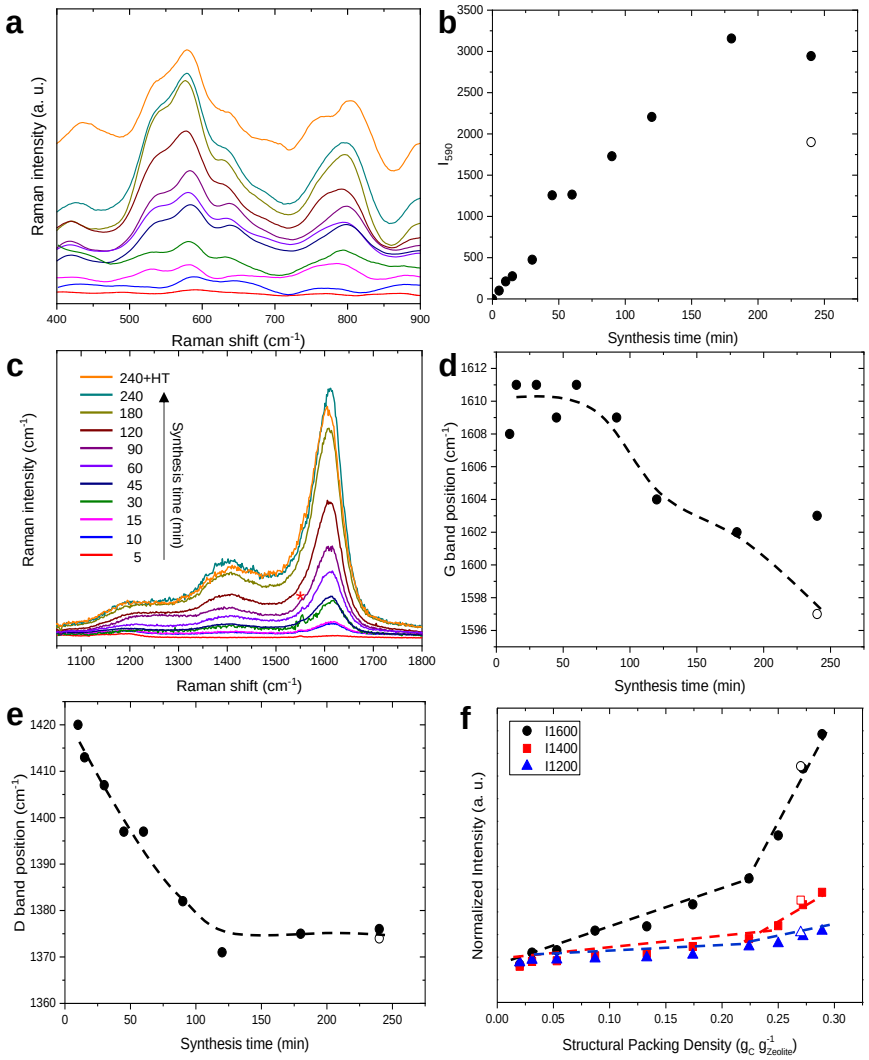

Figure 3. a) Normalized Raman spectra recorded at 532 nm (**Figure S7**). b) Evolution of the intensity at 590 cm^{-1} as a function of the synthesis time from spectra recorded at 532 nm. The empty symbols correspond to the sample 240 min+HT. c) Normalized Raman spectra recorded at 266 nm of hybrid materials achieved after different syntheses times. d) Evolution of the position of G band as a function of the synthesis time from spectra recorded at 532 nm. e) Evolution of the position of D band as a function of the synthesis time from spectra recorded at 532 nm. f) Intensity of G, D and S bands centered at approximately 1610, 1400 and 1200 cm^{-1} as a function of the synthesis time (inferred from spectra recorded at 266 nm). Empty symbols correspond to the sample 240 min+HT.

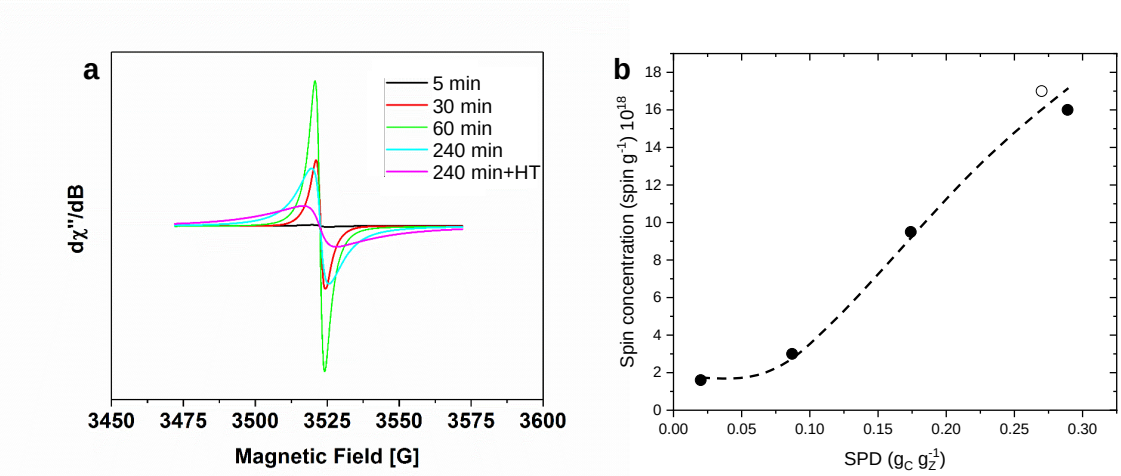

Figure 4. a) CW-EPR spectra of the hybrid materials achieved at different syntheses times. b) Evolution of the spin concentration as a function of the SPD. The empty symbol corresponds to the sample 240 min+HT.

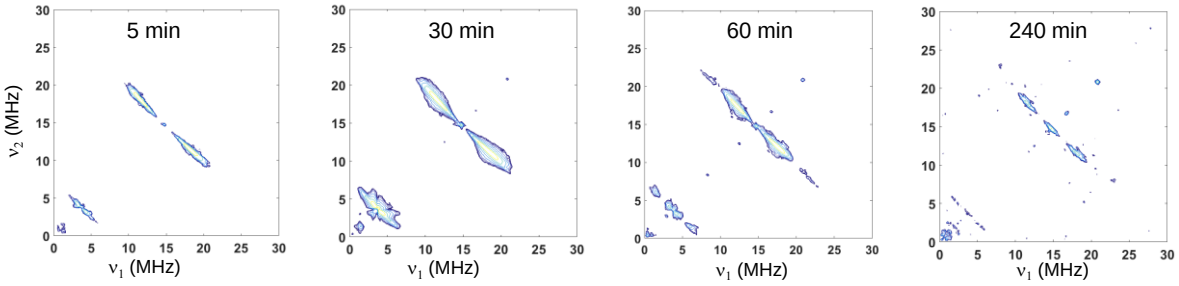

Figure 5. 2D-HYSCORE spectra of the hybrid materials recovered after 5, 30, 60 and 240 min.

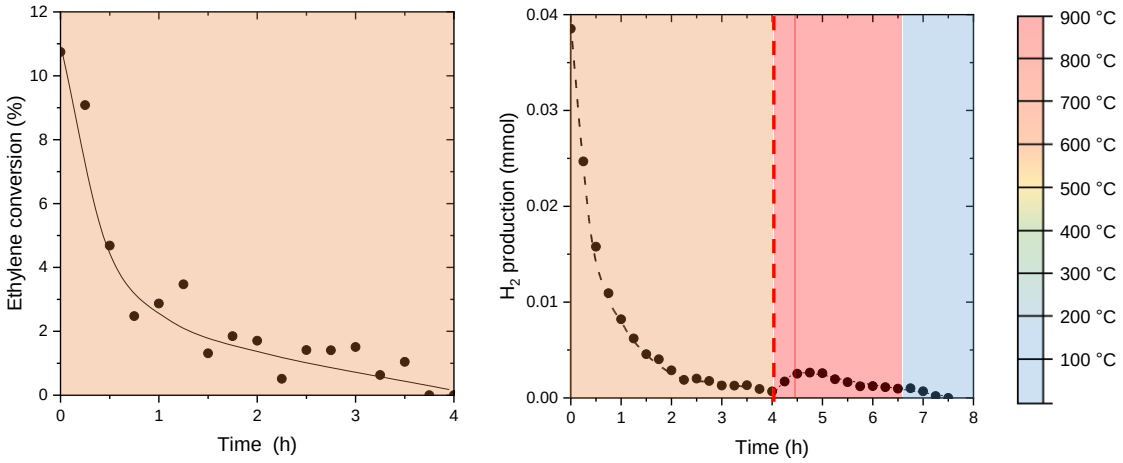

Figure 6. a) Evolution of the ethylene conversion as a function of the synthesis time. b) Hydrogen production as a function of the synthesis time. The red dashed line represents the time at which ethylene feeding was stopped and heat treatment was started. The scale bar represents the measured temperature in the reactor.

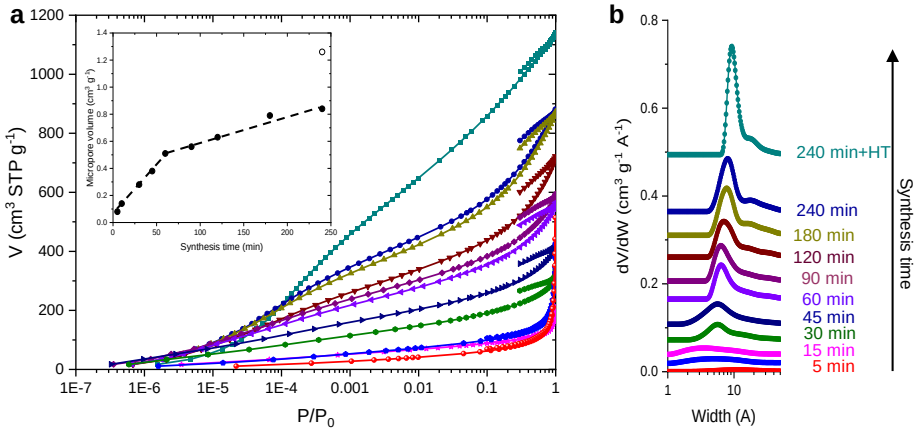

Figure 7. Nitrogen physisorption isotherms at 77 K (a) and NLDFT pore size distribution (b) for the carbon materials obtained after dissolution of the zeolite from the hybrid material achieved after different syntheses times. The insert in (a) represents the micropore volume as a function of the synthesis time. The empty symbol corresponds to the sample 240 min+HT.

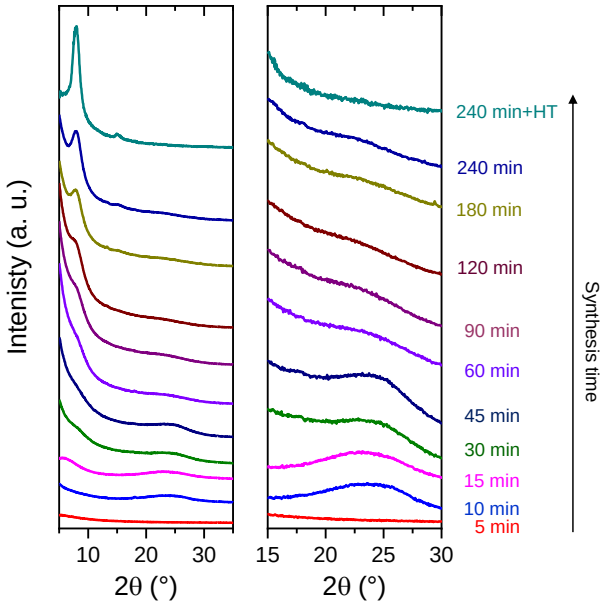

Figure 8. XRD powder patterns of carbon materials achieved at different syntheses times.

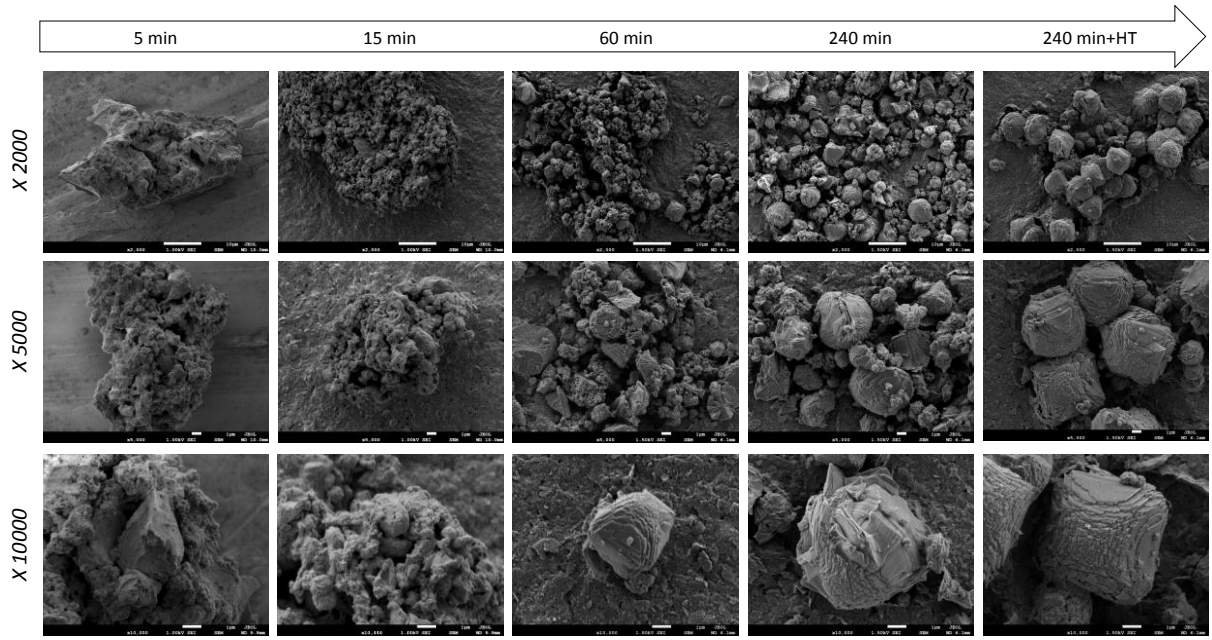

Figure 9. SEM images of the carbon materials achieved at different syntheses times.

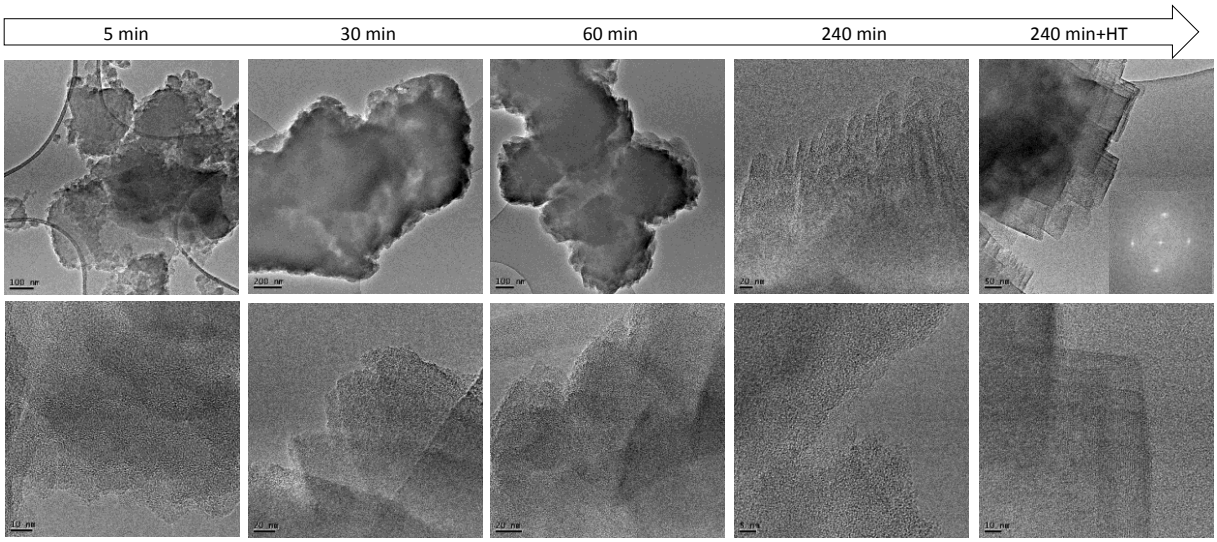

Figure 10. TEM images of carbon materials achieved at different syntheses times.

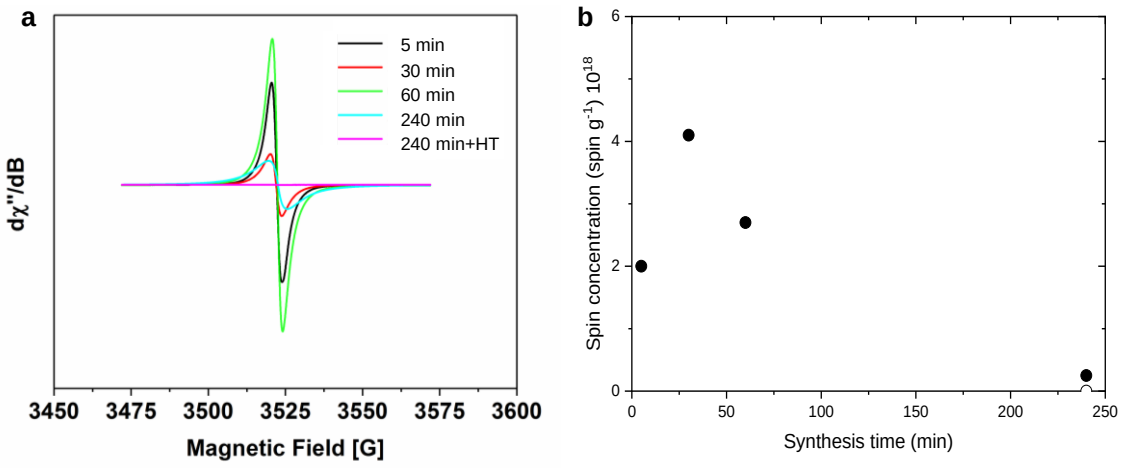

Figure 11. a) CW-EPR spectra of carbon materials obtained at different syntheses times. b) Spin concentration in the carbon materials as a function of the synthesis time.

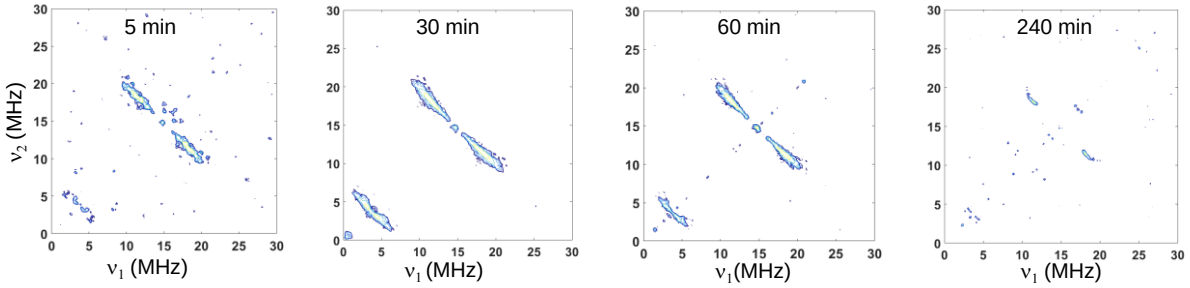

Figure 12. 2D HYSCORE spectra of the carbon materials recovered after 5, 30, 60 and 240 min.

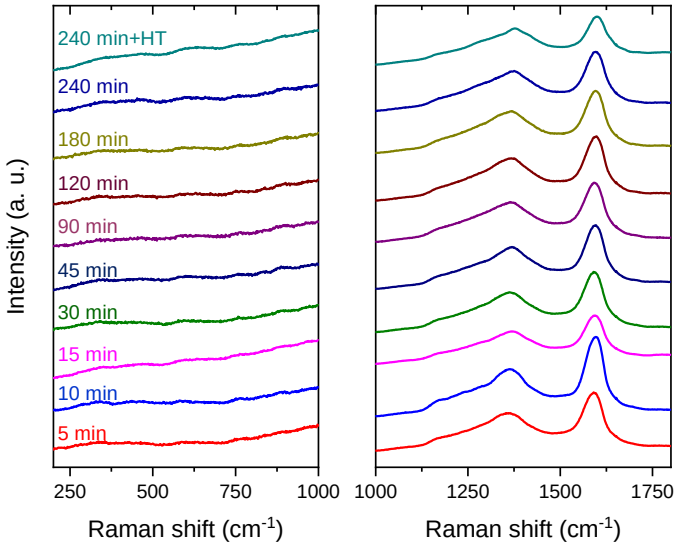

Figure 13. Raman spectra of carbon materials recorded at 532 nm.

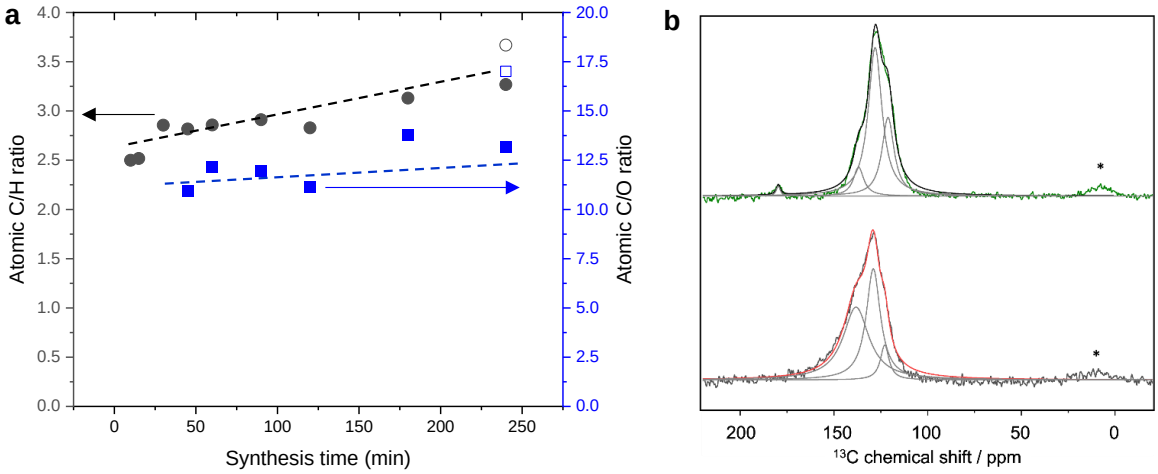

Figure 14. a) Atomic C/H (black) and C/O (blue) ratio of carbon materials as a function of the synthesis time. b) ^{13}C MAS NMR spectra of the hybrid material after heat treatment (red) and of the resulting carbon (green) and individual contributions fitted with DMFit [57]. Asterisks denote spinning sidebands. Empty symbols correspond to the sample 240 min+HT.

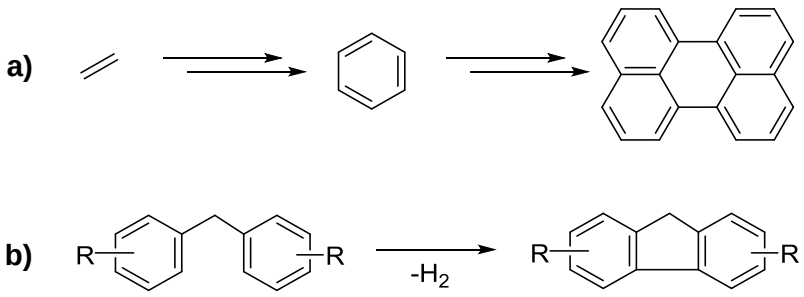

Scheme 1. Proposed mechanisms involved in ZTC synthesis. a) Nucleation and growth of polyaromatic hydrocarbons (PAHs) and b) PAHs condensation.